






Modelling of long-wave mid-infrared ultrashort pulse generation via difference frequency generation

XINYANG SU,^{1,*}  XIAOYU LUO,¹ QINGYU CHEN,¹ XINYUAN CHI,¹
ZHAOYANG TIAN,¹ BOLIN WANG,¹ QIAN CAO,^{2,5} 
SERGEY SARKISOV,³ AND SERGEY KOBTSEV⁴ 

¹School of Physical Science and Engineering, Beijing Jiaotong University, Beijing 100044, China

²School of Optical-Electrical and Computer Engineering, University of Shanghai for Science and Technology, Shanghai 200093, China

³Synchrotron Radiation Detector Laboratory, R&D Center “Advanced Electronic Technologies”, Tomsk State University, Tomsk 634050, Russia

⁴Division of Laser Physics and Innovative Technologies, Novosibirsk State University, Novosibirsk 630090, Russia

⁵cao.qian@usst.edu.cn

*xysu@bjtu.edu.cn

Abstract: In this paper, a model of generating mid-infrared (MIR) ultrashort laser pulse through difference frequency generation (DFG) is established. The pulse evolution relationship among the pump, signal, and idler pulses during the DFG process, as well as the effects of crystal length, pulse energy of the pump and signal lights, pulse width, and other factors on the characteristics of the MIR pulse are explored. Furthermore, through simulations from the time domain to the frequency domain, the spectral characteristics and angular distribution of MIR were analyzed. DFG experimental data are also presented to support the model.

© 2024 Optica Publishing Group under the terms of the [Optica Open Access Publishing Agreement](#)

1. Introduction

Ultrashort pulses in the long-wave MIR band have gathered significant attention due to their applications in spectroscopy, environmental sensing, and medical diagnostics, etc. This band, known as the “molecular fingerprint region” [1], is crucial for detecting and analyzing the absorption characteristics of various substances. Currently, the development of MIR ultrashort laser pulses is moving towards broader spectral ranges, narrower pulse widths, and higher average powers. Nonlinear optical frequency conversion has become a primary route to generating long-wave MIR ultrafast lasers, with DFG technology being widely applied for high repetition rate and high average power MIR generation [2]. Typically, the tuning of MIR wavelengths in DFG is contingent upon the tunability of the two-color near-infrared light at the input [3]. To date, there has been some progress in the experimental and simulation studies of long-wave MIR ultrafast lasers. Zhou et al. generated tunable mid-infrared pulses in the 7-18 μm range based on DFG, achieving an average power of up to 5.4 mW [4]. Su et al. achieved mid-infrared ultrashort pulses with a wavelength of 17.4 μm and a power of 2.5 mW by DFG [5]. Liu et al. achieved the generation of tunable mid-infrared pulses in the 6-20 μm wavelength range, and they found that changing the pump wavelength from 1.03 μm to 1.55 μm could increase the mid-infrared power by an order of magnitude due to the reduced GVM and an increased damage threshold for the nonlinear crystal used (GaSe) [6]. Huang et al. utilized a compact single-stage approach for generating LWIR seed by DFG of two-color chirped Ti:sapphire CPA output with a collinear geometry, which they refer to as chirped-pulse difference-frequency generation (CP-DFG), finally, mid-infrared pulses with an FWHM bandwidth of ~ 3 μm were

generated [7]. Regarding the quantum efficiency, employing longer wavelength ($>2\ \mu\text{m}$) pumps also enables higher output of the idler light. Cui et al. achieved long-wave MIR pulses with a power of 1.25 mW at $11\ \mu\text{m}$ through DFG using a MIR fluoride fiber laser as the driving source in their experiments, along with corresponding simulations, offering new possibilities for pulse generation in the MIR band [8]. Duda et al. achieved high-energy, few-cycle pulse generation in the long-wave infrared spectral region via difference-frequency generation (DFG) in GaSe and AgGaSe₂ nonlinear crystals. The final mid-infrared source contains up to $17\ \mu\text{J}$ of energy and covers a spectrum from $8.5\ \mu\text{m}$ to $14.5\ \mu\text{m}$. The driving source is a high-energy mid-infrared optical parametric chirped pulse amplifier (OPCPA) at a 1-kHz repetition rate where the signal and idler pulses are shaped for optimized DFG, resulting in a conversion efficiency above 2% [9]. Fuertjes et al. achieved idler pulses centered at $11.4\ \mu\text{m}$, with an energy of $65\ \mu\text{J}$ and a pulse duration of 185 fs via an OPCPA system. In this system, a femtosecond Cr: ZnS laser serves as the front-end, providing the seed for the $2\ \mu\text{m}$ pump and the $2.4\ \mu\text{m}$ signal pulses. For each amplification stage, the $2\ \mu\text{m}$ Ho:YLF regenerative amplifiers are used as the pump source [10]. In terms of theoretical simulation work on the mid-infrared laser generation via DFG, there is also some progress. Kaindl et al. demonstrated a simulation model with nonlinear coupled wave equations including the full dispersion of GaSe, demonstrating that the chirp of the pump pulse was shown to adjust the pulse duration and conversion efficiency in nonlinear processes, consistent with experimental observations [11]. Ishizuki et al. analyzed the pulse wavelength conversion characteristics in lithium niobate (LiNbO₃) waveguide nonlinear optical devices, including second harmonic generation, DFG, and sum frequency generation. By employing beam propagation method, variations in pulse width and the dependence of energy conversion efficiency on propagation distance are discussed, aiming to provide guidance for assessing and designing nonlinear optical device characteristics in ultra-high-speed optical signal processing [12]. Sharba et al. investigated a system combining second harmonic generation (SHG) with a low-gain optical parametric amplifier (OPA) aimed at enhancing the temporal contrast of laser pulses. Through comprehensive numerical simulations by solving nonlinear coupled wave equations, they considered various parameters influencing system performance, such as group velocity mismatch, beam divergence, and pulse chirp. They analyzed the impact of initial parameters of input pulses on system performance and explore how beam divergence alters the spectral and temporal characteristics of generated pulses. Even though this work is mainly on OPA, it still can provide some guidance for the simulation of DFG since OPA shares the same coupled wave equations with DFG [13]. Stepanov et al. demonstrated the generation of sub-cycle mid-infrared pulses at microjoule-level energies using an all-solid-state approach, addressing the current gaps in the sub-cycle optoelectronics field. Multi-cycle mid-infrared pulses were generated first via DFG, and then the pulses were compressed to sub-cycle durations through spectral broadening and careful dispersion compensation in optimized solid-state components. At the same time, they also did the simulation work by solving the three-dimensional time-dependent generalized nonlinear Schrödinger equation (GNSE) together with the rate equation of electron density to show the process mid-infrared supercontinuum generation and pulse compression [14]. Cao et al. simulated the power scalability of MIR frequency combs in high repetition rate DFG systems, with a particular focus on the power scalability of mid-infrared idler pulse energy, exploring the energy conversion efficiency under different pump and signal pulse conditions. The impact of group velocity mismatch (GVM) on energy scalability was assessed by comparing DFG driven by $1\ \mu\text{m}$ and $2\ \mu\text{m}$ pump pulses [15].

Previous experimental studies are mainly focused on the scaling up the average power of the MIR source or tuning its center wavelengths. Meanwhile, theoretical studies usually do not take a comprehensive parameter simulation for the generated MIR pulse. However, the pulse width, spectrum and angular distribution of the MIR are also important in practical applications such as temporal resolution, molecular detection and imaging. In this paper, we present a simulation work

for studying the pulse and spectrum evolution in the process of DFG process. Also, the angular distribution of the generated MIR power after the crystal is also simulated. Our experimental data on DFG is presented, which has good agreement with the model, presenting a more accurate and practical work.

2. Model

Through DFG process, the idler pulse ω_i is generated from two beams of light with frequencies ω_p and ω_s , where the two input pulses are the pump pulse and the signal pulse. Within a nonlinear optical crystal, the three beams overlap and interact, resulting in the conversion of energy from the pump pulse to the signal and idler pulses, as illustrated in Fig. 1.

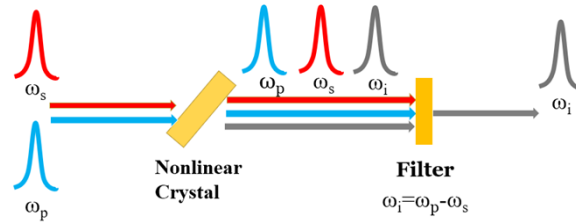


Fig. 1. Schematic diagram of DFG

In Fig. 1, three optical pulses—pump pulse ω_p , signal pulse ω_s and idler pulse ω_i —interact within a second-order nonlinear crystal, where $\omega_p > \omega_s > \omega_i$. This process results from the excitation of the second-order polarization $P^{(2)}$ oscillating at frequency $\omega_p - \omega_s$ [16].

Starting from the principle of energy conservation, the frequency of the idler light is the difference between the frequencies of the pump and the signal light. For three interacting light fields, the phase mismatch Δk under collinear conditions is the magnitude of the pump light field corresponding the wave vector k_p minus the sum of the magnitudes of the signal light field corresponding wave vectors k_s and k_i for the idler light. In the plane wave approximation, to ensure efficient energy transfer, the three waves must be phase-matched, implying that $\Delta k = 0$. At this condition, energy is precisely transferred from the pump light field to the signal and idler light fields. Specifically, the perfect phase matching under the collinear condition of plane waves is:

$$n_i \omega_i = n_p \omega_p - n_s \omega_s \quad (1)$$

where n represents the frequency-dependent refractive indices of the nonlinear optical crystal for the three optical fields. In birefringent crystals, the refractive index is dependent on the polarization state of the incident light beams. By adjusting the refractive index under the proper orientation of the crystal optical axis relative to the polarized pump and signal lights, the three interacting fields are phase-matched. For the type-I phase matching of DFG, it is achieved for the polarization orientations of the high frequency pump, low frequency signal and idler radiations being e-wave, o-wave, and o-wave, respectively [17]. GaSe crystal has been widely utilized in experimental studies of MIR lasers via DFG due to its high nonlinear coefficient (54 pm/V) and broad spectral transparency range (0.65-20 μm). Thus, it is selected as the preferred crystal for DFG simulation, with its dispersion equation (Sellmeier equation) presented as follows [18]:

$$\left. \begin{aligned} n_o^2 &= 10.6409 + \frac{0.3788}{\lambda^2 - 0.1232} + \frac{7090.7}{\lambda^2 - 2216.3} \\ n_e^2 &= 8.2477 + \frac{0.2881}{\lambda^2 - 0.1669} + \frac{4927.5}{\lambda^2 - 1990.1} \end{aligned} \right\} \quad (2)$$

where the n_o , n_e are the refractive index of ordinary wave and extraordinary wave, and λ is in micrometers. The formula is only valid in the range $0.8 \mu\text{m} \leq \lambda \leq 1620 \mu\text{m}$.

Starting from the time domain and employing the spacial slowly varying amplitude approximation while neglecting higher-order dispersion, by changing the reference frame based on the pump light group velocity, the transient nonlinear coupled wave equation for DFG can be derived [15]:

$$\left. \begin{aligned} \frac{\partial A_s(z,\tau)}{\partial z} + \left(\frac{1}{v_{g,s}} - \frac{1}{v_{g,p}} \right) \frac{\partial A_s(z,\tau)}{\partial \tau} + \frac{i\beta_{2,s}}{2} \frac{\partial^2 A_s(z,\tau)}{\partial \tau^2} &= \frac{i\omega_s d_{eff}}{cn_s} A_i^* A_p e^{-i\Delta kz} \\ \frac{\partial A_i(z,\tau)}{\partial z} + \left(\frac{1}{v_{g,i}} - \frac{1}{v_{g,p}} \right) \frac{\partial A_i(z,\tau)}{\partial \tau} + \frac{i\beta_{2,i}}{2} \frac{\partial^2 A_i(z,\tau)}{\partial \tau^2} &= \frac{i\omega_i d_{eff}}{cn_i} A_s^* A_p e^{-i\Delta kz} \\ \frac{\partial A_p(z,\tau)}{\partial z} + \frac{i\beta_{2,p}}{2} \frac{\partial^2 A_p(z,\tau)}{\partial \tau^2} &= \frac{i\omega_p d_{eff}}{cn_p} A_s A_i e^{+i\Delta kz} \end{aligned} \right\} \quad (3)$$

where A_p , A_s and A_i are the complex amplitude of electric field of the pump, signal, and idler pulse, respectively. $v_{g,p}$, $v_{g,s}$ and $v_{g,i}$ represent the group velocities of the pump, signal, and idler pulse, respectively. ω_p , ω_s and ω_i correspond to the frequencies of the three wavelengths. $\beta_{2,p}$, $\beta_{2,s}$ and $\beta_{2,i}$ denote the group velocity dispersion (GVD) of the three wavelengths within the crystal material. The introduced delay time τ is defined as $\tau = t - z/v_{g,p}$, where d_{eff} is the effective nonlinearity coefficient. The equation does not take the Kerr effect into consideration since the real input peak power is usually under the critical power for self-focusing. The spatial walk-off effect is introduced to the equations according to the overlapping area of two beams in the coupled-wave equations led by this effect. The reduction in beam overlapping reduces the product between their light intensity, which can be taken into consideration by modifying the nonlinear coefficient d_{eff} . The equation is solved using the Fourier split-step and the fourth-order Runge-Kutta (RK4) algorithms.

When solving the time-domain nonlinear coupled wave equations, the split-step Fourier method is used and different approaches are adopted for calculating the effects dispersion and nonlinearity. The treatment of dispersion involves performing a Fast Fourier Transform (FFT) of its time-domain equation, solving for dispersion effects in the frequency domain, and subsequently carrying out an Inverse Fast Fourier Transform (IFFT) to revert the frequency domain back to the time domain. The treatment of nonlinearity employs a RK4 algorithm. After the sufficient number of cycles of separately computing the dispersion and nonlinearity parts, the information of the emitted pump and idler light in both time and frequency domains can be obtained.

As shown in Fig. 2, the solution to the coupled-wave equation is primarily conducted through the following loop. The initial pulse conditions for the pump and signal lights are input, here we have

$$\left. \begin{aligned} A_s(\tau, z = 0) &= E_s \operatorname{sech}(44/25 t_s \cdot \tau) \\ A_p(\tau, z = 0) &= E_p \operatorname{sech}(44/25 t_p \cdot \tau) \end{aligned} \right\} \quad (4)$$

where E_s and E_p are the peak amplitude of the signal and idler pulse, which can be calculated by the square root of their peak powers. t_s and t_p are the pulse widths of the signal and pump pulse. τ is the range of the time window, the initial two pulses can be seen as sech^2 pulses, since the constant 44/25 in this expression is to normalize the time scale of the pulse, ensuring that the equation accurately describes the shape of the sech^2 pulse. Furthermore, the wavelength λ_p , λ_s , pulse energy Q_p , Q_s and pulse width t_p , t_s are also set as well. Then, specific initial values for dispersion and nonlinear effects are input. After setting the window width to τ and calculating the number of sampling points, the parameters of the crystal are inputted, where the crystal length L is divided into n segments. The dispersion and nonlinear parts are calculated separately, repeatedly computing until the crystal length reaches the inputted crystal parameters. This will yield a complex matrix $A_j (j = p, s, i)$ from which the corresponding power $P_j = |A_j|^2$ can be represented by summing the absolute value of complex number in the row of matrix.

The FFT algorithm is utilized for solving the nonlinear coupled wave equation. This model is capable of simulating the pump, signal, and idler pulses simultaneously during the DFG process, where each operates independently yet influences one another. Additionally, by adjusting initial

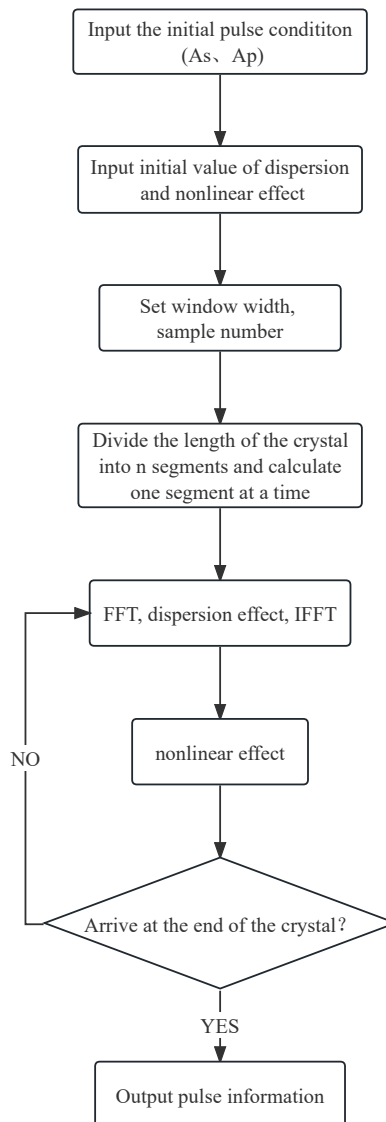


Fig. 2. Flow chart of algorithm for solving nonlinear coupled wave equation

conditions such as pulse width and wavelength, the desired idler light band can be obtained. Following the literature [5], pump and signal pulses with wavelengths of 1024 nm and 1088 nm, respectively, are set as the initial dual pulses injected into the crystal. Their pulse energies and widths are 24.6 nJ, 900 fs, and 12.3 nJ, 600 fs, respectively. From the previously mentioned method for calculating the frequency of the idler pulse, its wavelength is calculated to be 17.4 μm . Due to the group velocity mismatch between the pump and signal lights, the signal pulse always precedes the pump. To ensure maximum overlap time within the crystal, the pump pulse is set to lead the signal pulse by half the total walk-off time in the crystal at the input port, and all pulses are considered as Fourier transform-limited pulses. By changing the crystal length, idler pulses with different pulse energies and shapes are achieved.

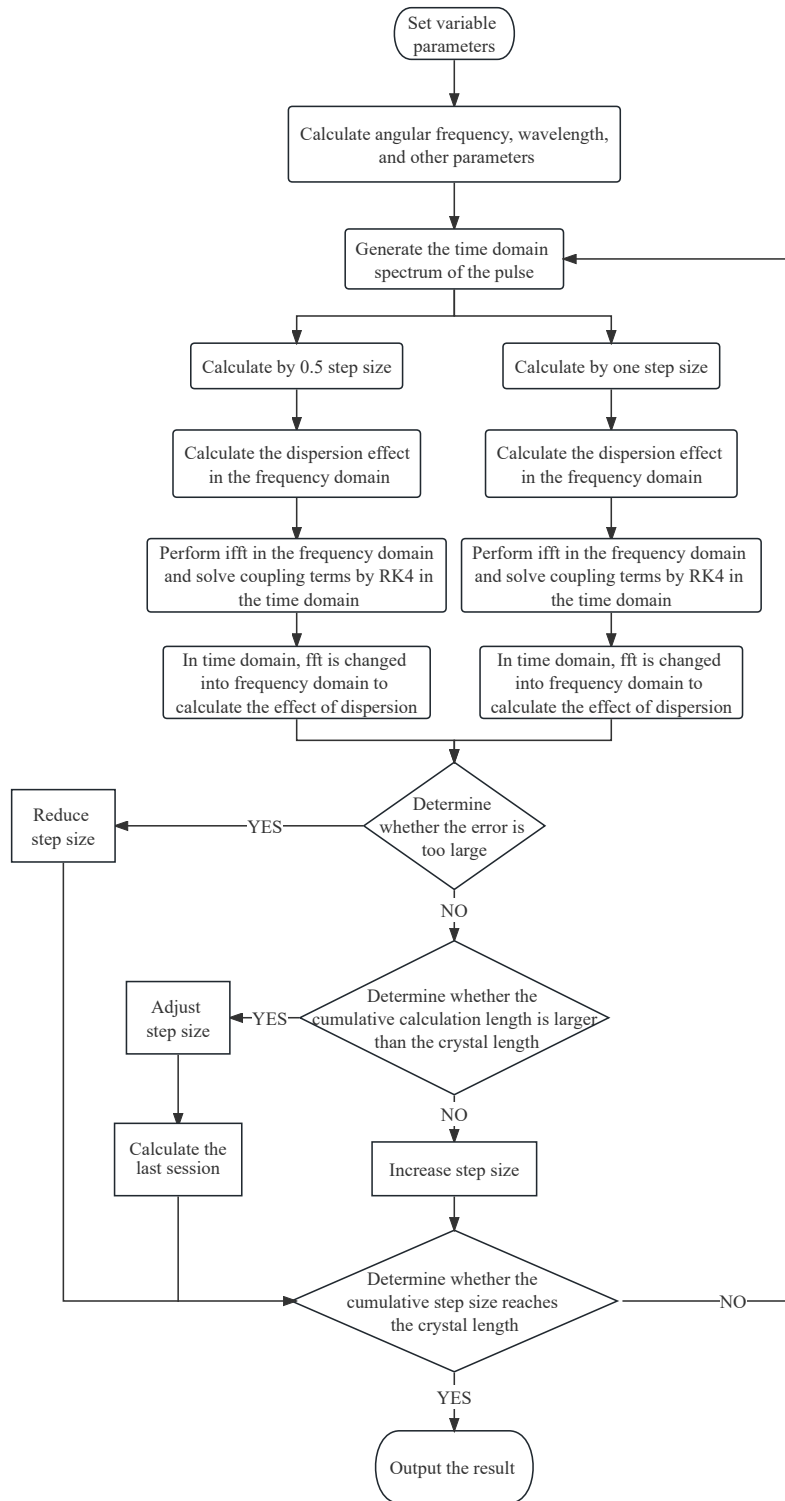


Fig. 3. Algorithm flow chart of mid-infrared spectrum simulation

Moreover, Fig. 3 illustrates the specific algorithmic flow. After initializing the parameters, the crystal length is divided into several segments. Within each step length, the coupling terms and dispersion effects are calculated separately in the time and frequency domains. An adaptive computation is used in the iterative method to modify the step size dz in real-time, with half a step being $0.5 \cdot dz$. The final computations yield the ultimate shape of the pulse, its energy distribution, and its time-frequency domain characteristics. Through FFT, the pulse in the time domain is converted to the frequency domain, allowing for the analysis of the spectral components of the pulse. Before calculating nonlinear effects, the pulse is transformed from the time domain to the frequency domain to solve ordinary differential equations, which facilitates calculating the effects of dispersion. After processing for dispersion and frequency domain treatment of nonlinear interactions, IFFT is used to convert the processed pulse information back to the time domain for the analysis of the time-domain characteristics of the pulse.

For the simulation of spatial distribution, the Morris et al. proposed a theoretical model based on the spatial distribution of MIR generated by DFG of Gaussian beams [19,20]. According to this model, the input focused beam in the nonlinear optical crystal is set as a Gaussian beam. Under Type I phase matching conditions and considering boundary effects, the expression for the forward idler light field outside the crystal can be obtained:

$$\frac{dP_{\pm}(\theta, \phi)}{d\Omega} = \frac{c}{2\pi} \cos^2\theta |\vec{E}_{T\pm}(\vec{k}_T)|^2 \quad (5)$$

$$\vec{k}_T = \frac{\omega}{c} \sin\theta (\hat{x}\cos\phi + \hat{y}\sin\phi) \quad (6)$$

where the $P_{\pm}(\theta, \phi)$ is the forward and backward mid-infrared power generated by DFG; θ, ϕ are the polar angle and azimuth angle, respectively; $\vec{E}_{T\pm}$ is the generated field outside the crystal; the subindices “+” and “-” denote forward and backward propagating directions; $\vec{E}_{T\pm}$ is derived by solving the wave equations for the MIR generation by DFG where the two input beams were set as Gaussian beams rather than plane-wave beams [19,20].

3. Simulation results and discussions

Based on the aforementioned simulation model and algorithm, we present the initial conditions for the simulation as shown in Table 1. Before some simulation results are shown, here an introduction of the experimental setup is also provided. A watt-level two-color (1024 and 1088 nm) synchronous pulses are generated through an CPA set up, and then the two-color pulses are orthogonally polarized through an periscope system, and finally, they are focused into an GaSe crystal to achieve mid-infrared generation. The focused beam spot radius are selected to be 17.8 μm , 26.7 μm , 35.6 μm , and 80.1 μm , respectively. A thermal power meter with a Germanium filter was used to measure the generated mid-infrared power. A 50-grooves/mm monochromator with a nitrogen-cooled mercury cadmium tellurium (HgCdTe) detector was used to measure the spectrum of the MIR. The angular distribution of the generated MIR source was scanned across the beam in two perpendicular directions with the HgCdTe detector installed on the translation stage. Finally, mid-infrared pulses with an average power of 2.5 mW and a centre wavelength of 17.4 μm are generated. The initial condition is referenced through the work in [5].

In Fig. 4, we obtain the pulse shapes and energies of the three waves with different crystal lengths, wherein Fig. 4(a) shows the idler pulse shape and energy with different crystal lengths, and Fig. 4(b) shows the pump, signal and idler pulse energy with different crystal lengths. As can be seen in the figure, the energy is transferred from the pump pulse to both the signal and the idler pulses. With the increase of the crystal length, the pump pulse energy gradually decreases, and the signal and the idler pulse energies gradually increase. When the crystal length is 0.5 mm, the obtained idler optical pulse energy is only 31.2 pJ. When the length increases from 0.5 mm to 2 mm, the pulse energy increases almost linearly as the crystal length increases, but when the

Table 1. Simulation initial parameters

Physical quantity	Data
Time interval dt / s	10^{-15}
Pump wavelength / nm	1024
Pump pulse energy / nJ	24.6
Pump pulse width / fs	900
Signal wavelength / nm	1088
Signal pulse energy / nJ	12.3
Signal pulse width / fs	600
Idler pulse wavelength / nm	17400

length exceeds 2 mm, the pulse energy is close to saturation. When the length exceeds 3 mm, the pulse energy does not grow with the length. This is mainly because the group velocity walk-off effect causes the pump and the idler pulses to be almost separated at 3 mm of the crystal, and finally the DFG process no longer continues. It is also can be noticed that the calculated idler pulse energy is 78 pJ when the crystal length is 1 mm, meanwhile the measured the idler pulse energy is around 40 pJ in the real experiment. The simulation result is a little bit higher than the experimental one since the model does not considers the absorption of the crystal and the effect of the divergence angle on the interaction of the three beams in the crystal, which leads to more loss on the the mid-infrared generation.

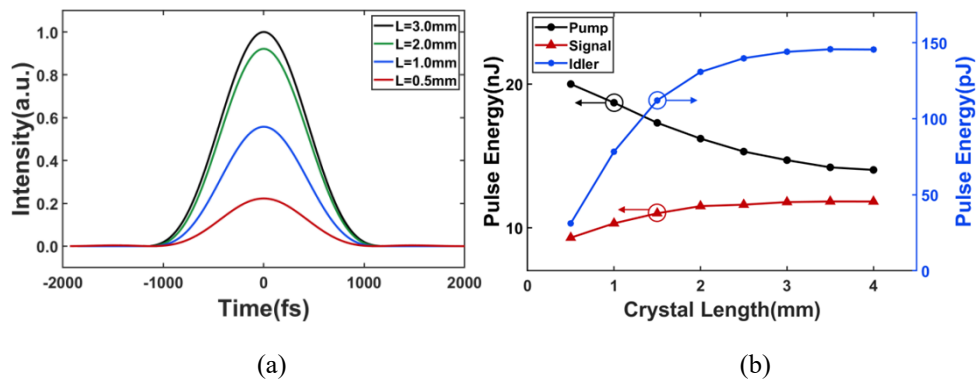


Fig. 4. Effect of the GaSe length on (a) the idler pulse shape (b) the pulse energy of pump, signal and idler

As shown in Fig. 5, the crystal length also affects the idler pulse width. When the crystal length increases from 0.5 mm to 4 mm, then the idler pulse width increases from 940 to 987 fs due to group velocity dispersion.

Figure 6 shows the evolution trend of the pump, signal and idler pulses in a 5 mm GaSe crystal during the DFG process. This dynamic process is represented by a two-dimensional top-view diagram, where the x-axis indicates the time domain and the y-axis represents the crystal length, with different colors representing the intensity of optical power. From the figure, we can see that the pump pulse undergoes only a slight reduction in energy after traversing the crystal, whereas the signal pulse energy exhibits a more pronounced increase. When the pump and signal pulses are phase-matched within the crystal, the power of the idler pulse increases with the length of the crystal. However, as group velocity dispersion results in temporal walk-off of the pulses, the growth in energy of the idler pulse will experience a stagnation.

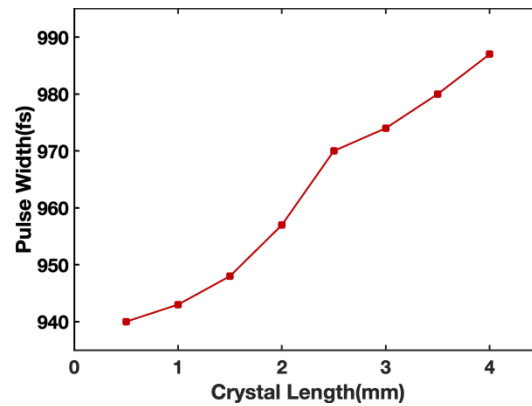


Fig. 5. Effect of the length on the idler pulse width

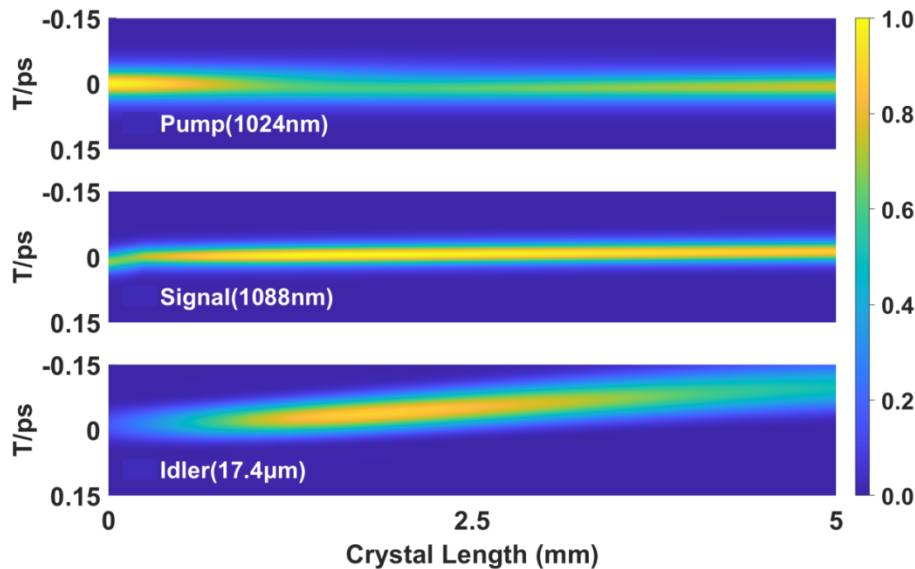


Fig. 6. Evolution stereogram of three waves of DFG in 5 mm thick GaSe crystal

At the crystal length of 1 mm, the initial and final states of the pulses are taken from the above evolution stereogram, where the relative pulse intensity profile of the idler pulse is magnified by 80 times to be more obvious. Due to the influence of group velocity mismatch, the signal pulse travels faster than the pump pulse by 44 fs when passing through a 1 mm GaSe crystal. Thus, when the pump pulse is used as the reference frame, the pump pulse is set to travel earlier than signal light by 22 fs in advance at the input end, which is just half of the total time walk-off. Therefore, the signal pulse will pass through the peak position of the pump pulse in the crystal, and finally leading the pump by 22 fs at the output end. Considering the Fresnel reflection loss, during the input-to-output process, the pump light energy is decreased from 20.8 nJ to 18.7 nJ. The signal light energy is increased from 8.6 nJ to 10.4 nJ. Furthermore, the idler pulse leads the pump pulse by 140 fs. However, because the pump pulse width is wide and still has a large pulse energy, the three pulses still remain in an overlapping state, as shown in Fig. 7.

Figure 8 depicts the variation in the idler pulse energy produced by the DFG process as a function of the input pulse energies of the pump and signal pulses, with the crystal length set at 1

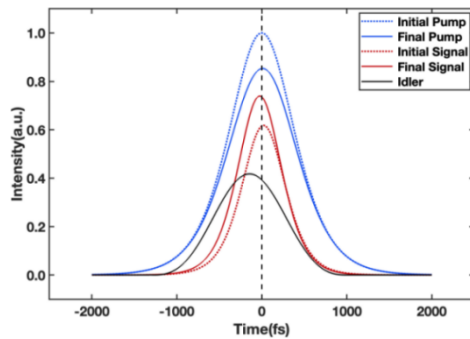


Fig. 7. DFG process at 1-mm-thick GaSe. Pulse profile at both the input and output position. The idler in the graph is magnified by a factor of 80.

mm and the focused spot radius at $15\ \mu\text{m}$, sequentially fixing the signal and then the pump light. When the input pulse energy of the signal pulse is fixed, as shown in Fig. 8(a), the pulse energy of the idler light increases linearly with the input pump pulse energy between 0.1 nJ and 100 nJ. Between 100 nJ and 1000 nJ, the growth rate of the idler pulse energy increases nonlinearly. At this time, the DFG process is within the optical parametric amplification region [6]. When the input pulse energy of the pump light is fixed at 0.1 nJ, 1 nJ and 10 nJ, the pulse energy of the idler light increases linearly with the signal light input pulse energy increasing between 0.1 nJ and 100 nJ. However, between 100 nJ and 1000 nJ, the idler pulse energy decreases. Therefore, it can be seen that under the condition of a fixed signal light power, the pump light power plays a decisive role in enhancing the MIR (idler light) power, while an increase in signal light power tends to saturate the MIR power. The damage threshold of the crystal is related to the repetition rate [21], and higher repetition rate results in lower damage thresholds for the crystal. Thus, OPA usually works in low repetition laser system. In such a low repetition rate laser system, it is more possible to enter the optical parametric amplification region by increasing the energy of the incident pump pulse, since it allows the pump pulse energy to reach μJ or mJ level.

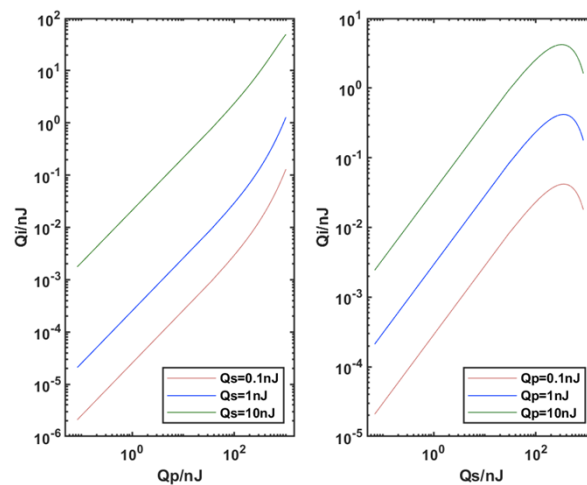


Fig. 8. The energy of the idler pulse output at different (a) Q_p and (b) Q_s of DFG

Figure 9 presents the variation in idler pulse energy when the incident pump and signal pulses are set to the same pulse width and then both are simultaneously increased. It is observed that

the idler pulse energy reaches the maximum at around 113 fs, indicating that the conversion efficiency of the MIR of the DFG scheme is also at its highest. The pulse width at this point provides optimal temporal overlap of the pump and signal pulses. This means that the temporal overlap of the two light pulses in the crystal is maximized, allowing the greatest amount of energy to be converted into the idler light under phase-matching conditions. However, as the pulse width continuously increases, the energy of the idler pulse decreases sharply. This is because the efficiency of the nonlinear effect is related to the intensity of the light, and as the pulse width increases, the peak power decreases, resulting in reduced efficiency of the nonlinear effect and consequently less energy converted the idler pulse.

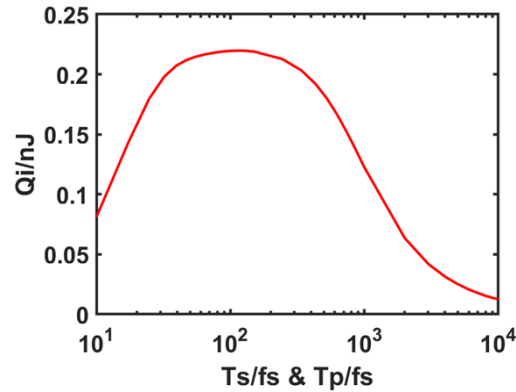


Fig. 9. Relationship between pulse width and energy of idle pulse

Figure 10 presents a frequency-domain simulation of the DFG spectrum. By fixing the output idler wavelength at 17.4 μm and considering focused beam radii of 17.8 μm , 26.7 μm , 35.6 μm , and 80.1 μm , a comparison is drawn between frequency-domain simulation data for a 1 mm crystal and the data obtained experimentally. In all cases, the simulation results show consistency with experimental data, indicating that the simulation model used can effectively emulate the physical processes under experimental conditions. From the simulation and experimental data, we can draw the conclusion that the focused beam radius does not affect the shape of the MIR spectrum.

Figure 11(a) displays the influence of crystal length (ranging from 0.5 mm to 3.0 mm) on the idler light spectrum. The thinnest crystal (0.5 mm) exhibits the widest spectrum. From 0.5 mm to 3.0 mm crystal length, spectral bandwidths are 0.93 μm , 0.86 μm , 0.80 μm , 0.74 μm , 0.68 μm , 0.5 μm , respectively. Meanwhile, thicker crystals correspond to a narrower phase-matching bandwidth and narrower spectrum. This is because effective energy exchange through parametric nonlinear interactions is only possible when phase matching is achieved. The acceptance bandwidth primarily depends on the phase mismatch range allowed by the crystal length [22]. Specifically, the shorter the crystal length, the greater the permissible phase mismatch. Furthermore, phase matching can only occur within a limited bandwidth, which is related to the group velocity mismatch of the interacting waves. In Fig. 11(b), the effect of the focusing spot radius (from 20 μm to 100 μm) on the generated idler light spectrum is presented, showing that the full width at half maximum (FWHM) is not affected by the radius of the focusing spot, remaining at 0.86 μm .

With a fixed output wavelength of 18 μm and focusing spot radii of 17.8 μm , 26.7 μm , 35.6 μm , and 80.1 μm , the spatial angular distribution of the MIR intensity can be calculated, as shown in Fig. 12. Due to axial phase mismatch, the intensity exhibits a hollow-cone distribution pattern, and the smaller the focusing spot radius relative to the wavelength, the more pronounced the central

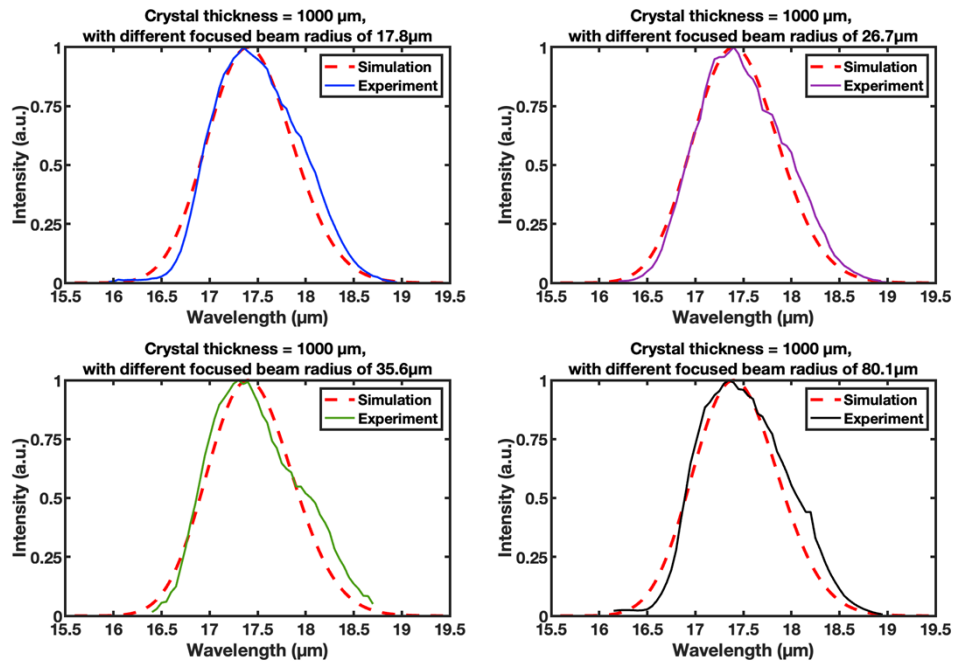


Fig. 10. Comparison of mid-infrared spectral intensities of different focused beam radii in the 1000 μm crystal

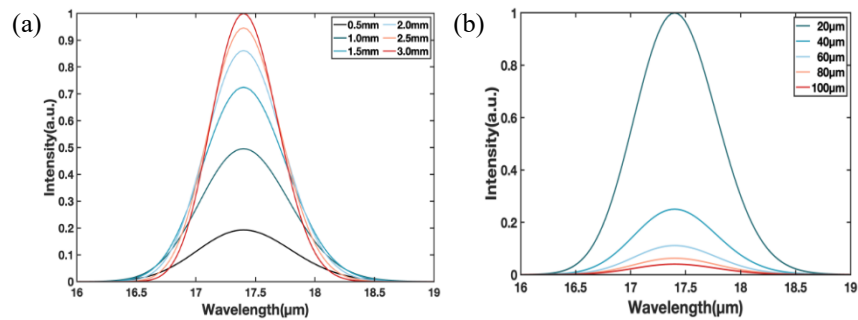


Fig. 11. Spectral changes at different (a) crystal lengths (b) focused spot radius, respectively

intensity dip becomes. Additionally, with a fixed focusing spot size, the larger the wavelength, the more apparent the dip. Current nonlinear optical gas experiments have provided support for this conclusion [23]. The simulation results are also compared with the experimentally measured beam profiles. As shown in Fig. 12, where z represents the measurement positions located at distances of 37, 46 and 55 mm behind the crystal, respectively. This figure contains both newly plotted figures (pure simulation results) and previously published figures (measured results). The left column of the figures are newly plotted, and the right column of the figures are previously published in [5]. From what we obtained in our experiment, we did not image the MIR spot and so only measured the two perpendicular diameters. Within the noise of our measurements, the two dimensions are equal and so. Consequently, we think that the idler beam is circularly symmetric. Furthermore, results of the measured beam profile in [8,10,24,25] also show almost circularly symmetric profile result like us. Thus, the model we used is a one-dimensional model, but we achieved a three-dimensional profile by rotating a one-dimensional curve around a fixed

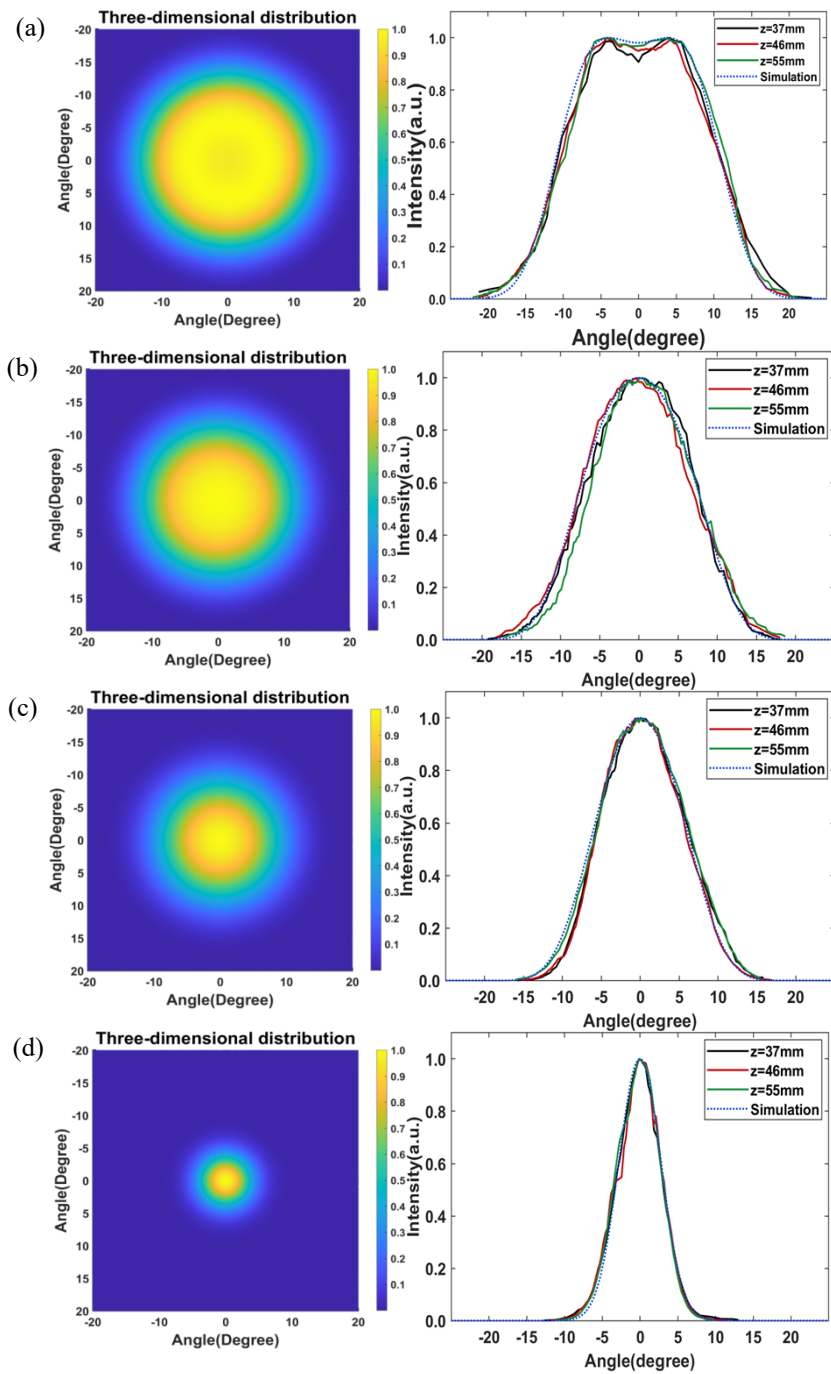


Fig. 12. Comparison of the theoretical and experimental results of the mid-infrared spatial distribution when the GaSe crystal length is 1 mm, the output wavelength is $18\ \mu\text{m}$, and the focusing spot radius is (a) $17.8\ \mu\text{m}$ (b) $26.7\ \mu\text{m}$ (c) $35.6\ \mu\text{m}$ and (d) $80.1\ \mu\text{m}$, respectively

axis as shown in the left part of Fig. 12. When the beam radius is 17.8 μm , the beam profile of the MIR beam exhibits a central dip, indicating the occurrence of conical emission when the beam size approaches the scale of the MIR wavelength [5].

4. Conclusion

Through detailed simulation analysis of the DFG process for MIR ultra-short pulse lasers, several conclusions have been reached. Firstly, the length of the crystal significantly impacts the shape, energy, width, and bandwidth of the idler pulse. Secondly, the energies of the pump and signal pulses both play crucial roles in enhancing the energy of the MIR pulse. Particularly under the drive of μJ -level pump pulse energies, the DFG transitions from a regular operating state to an OPA state, with the idler pulse energy shifting from linear to exponential growth, significantly increasing the MIR conversion efficiency of the DFG scheme. It is also observed that due to the group velocity dispersion effects, the idler pulse energy first increases and then plateaus with increase of the crystal length. Furthermore, based on the validation of MIR spectral simulation model by experimental data, the MIR spectra under different crystal lengths and various focusing spot radii are compared. Last but not least, a Gaussian beam-based DFG model is established to show the angular distribution of MIR intensity outside the crystal. The results of this study are of significant importance for the design and optimization of DFG MIR ultrafast laser sources and provide a theoretical foundation for future experimental research and applications. We will further improve the model to be closer to the experimental results by considering the effects of crystal absorption and the divergence angle of each beam.

Funding. High-end Foreign Experts Recruitment Plan of China (G2023104003L); National Natural Science Foundation of China (12275017, 61935010); Decree of the Government of the Russian Federation (No. 075-15-2022-1132 of 01 July 2022).

Disclosures. The authors declare that there are no conflicts of interest related to this article.

Data availability. Data underlying the results presented in this paper are not publicly available at this time but may be obtained from the authors upon reasonable request.

References

1. X. Su, R. Zhu, B. Wang, *et al.*, "Generation of 8–20 μm Mid-Infrared Ultrashort Femtosecond Laser Pulses via Difference Frequency Generation," *Photonics* **9**(6), 372 (2022).
2. M. Seidel, *A New Generation of High-Power, Waveform Controlled, Few-Cycle Light Sources* (2019).
3. S. Kobtsev, "Methods of Radiation Wavelength Tuning in Short-Pulsed Fibre Lasers," *Photonics* **11**(1), 28 (2023).
4. G. Zhou, Q. Cao, F. X. Kärtner, *et al.*, "Energy scalable, offset-free ultrafast mid-infrared source harnessing self-phase-modulation-enabled spectral selection," *Opt. Lett.* **43**(12), 2953–2956 (2018).
5. X. Su, M. Lyu, T. Hoang, *et al.*, "Investigation of long wavelength mid-infrared generation in the tight focusing limit," *Opt. Express* **27**(18), 24945–24952 (2019).
6. Y. Liu, J. Zhao, Z. Wei, *et al.*, "High-power, high-repetition-rate tunable longwave mid-IR sources based on DFG in the OPA regime," *Opt. Lett.* **48**(4), 1052–1055 (2023).
7. H. Huang, X. Xiao, M. Burger, *et al.*, "Ultra-broadband long-wave-infrared pulse production using a chirped-pulse difference-frequency generation," *Opt. Lett.* **47**(13), 3159–3162 (2022).
8. Y. Cui, H. Huang, Y. Bai, *et al.*, "Long-wave-infrared pulse production at 11 μm via difference-frequency generation driven by femtosecond mid-infrared all-fluoride fiber laser," *Opt. Lett.* **48**(7), 1890–1893 (2023).
9. M. Duda, L. von Grafenstein, M. Bock, *et al.*, "10- μJ few-cycle 12- μm source based on difference-frequency generation driven by a 1-kHz mid-wave infrared OPCPA," *Opt. Lett.* **47**(11), 2891–2894 (2022).
10. P. Fuertjes, M. Bock, L. von Grafenstein, *et al.*, "Few-cycle 65- μJ pulses at 11.4 μm for ultrafast nonlinear longwave-infrared spectroscopy," *Optica* **9**(11), 1303–1306 (2022).
11. R. A. Kaindl, F. Eickemeyer, M. Woerner, *et al.*, "Broadband phase-matched difference frequency mixing of femtosecond pulses in GaSe: Experiment and theory," *Appl. Phys. Lett.* **75**(8), 1060–1062 (1999).
12. H. Ishizuki, T. Suhara, H. Nishihara, *et al.*, "Numerical analysis of ultra-short pulse wavelength conversion characteristics of LiNbO₃ waveguide nonlinear-optic devices," *Electron Comm Jpn Pt II* **86**(3), 11–20 (2003).
13. A. B. Sharba, G. Nersisyan, M. Zepf, *et al.*, "Comprehensive numerical modelling of the performance of a second harmonic generation stage coupled with a low-gain optical parametric amplifier," *Opt. Express* **24**, 5212–5234 (2016).
14. E. A. Stepanov, A. A. Lanin, A. A. Voronin, *et al.*, "Solid-State Source of Subcycle Pulses in the Midinfrared," *Phys. Rev. Lett.* **117**(4), 043901 (2016).

15. Q. Cao, F. X. Kärtner, G. Chang, *et al.*, “Towards high power longwave mid-IR frequency combs: power scalability of high repetition-rate difference-frequency generation,” *Opt. Express* **28**(2), 1369–1384 (2020).
16. G. New, *Introduction to Nonlinear Optics* (Cambridge University Press, Cambridge, 2011).
17. C. Manzoni and G. Cerullo, “Design criteria for ultrafast optical parametric amplifiers,” *J. Opt.* **18**(10), 103501 (2016).
18. K. Kato, F. Tanno, N. Umemura, *et al.*, “Sellmeier and thermo-optic dispersion formulas for GaSe (Revisited),” *Appl. Opt.* **52**(11), 2325–2328 (2013).
19. J. R. Morris and Y. R. Shen, “Far-infrared generation by picosecond pulses in electro-optical materials,” *Opt. Commun.* **3**(2), 81–84 (1971).
20. J. R. Morris, “Optical difference frequency generation of far infrared radiation,” United States, (1977).
21. C. Zhu, V. Dyomin, N. Yudin, *et al.*, “Laser-Induced Damage Threshold of Nonlinear GaSe and GaSe:In Crystals upon Exposure to Pulsed Radiation at a Wavelength of 2.1 μm ,” *Appl. Sci.* **11**(3), 1208 (2021).
22. J. D. Ma, W. Hao-Yu, L. Qiao, *et al.*, “Fiber-type difference frequency generation infrared optical frequency comb based on the femtosecond pulses generated by a mode-locked fiber laser,” *Acta Phys. Sin.* **67**(9), 094207 (2018).
23. Y. S. You, T. I. Oh, K. Y. Kim, *et al.*, “Off-Axis Phase-Matched Terahertz Emission from Two-Color Laser-Induced Plasma Filaments,” *Phys. Rev. Lett.* **109**(18), 183902 (2012).
24. I. Pupeza, D. Sánchez, J. Zhang, *et al.*, “High-power sub-two-cycle mid-infrared pulses at 100 MHz repetition rate,” *Nat. Photonics* **9**(11), 721–724 (2015).
25. Q. Wang, J. Zhang, A. Kessel, *et al.*, “Broadband mid-infrared coverage (2–17 μm) with few-cycle pulses via cascaded parametric processes,” *Opt. Lett.* **44**(10), 2566–2569 (2019).